IEEE Access
Multidisciplinary ⋮ Rapid Review ⋮ Open Access Journal

Received April 10, 2022, accepted April 23, 2022, date of publication May 4, 2022, date of current version May 11, 2022.

Digital Object Identifier 10.1109/ACCESS.2022.3171916

Exploiting the Multiscale Information Fusion Capabilities for Aiding the Leukemia Diagnosis Through White Blood Cells Segmentation

NADEEM AKRAM[1], SHARJEEL ADNAN[1], MUHAMMAD ASIF[1], SYED MUHAMMAD ALI IMRAN[2], MUHAMMAD NAVEED YASIR[3], RIZWAN ALI NAQVI[4], AND DILDAR HUSSAIN[5]

[1]Department of Primary and Secondary Health Care, Government of Pakistan, Lahore 54000, Pakistan
[2]Department of Computer Science, University of Agriculture, Faisalabad 38000, Pakistan
[3]Department of Computer Science, University of Narowal, Narowal 51600, Pakistan
[4]Department of Unmanned Vehicle Engineering, Sejong University, Seoul 05006, South Korea
[5]School of Computational Sciences, Korea Institute for Advanced Study (KIAS), Seoul 02455, South Korea

Corresponding authors: Rizwan Ali Naqvi (rizwanali@sejong.ac.kr) and Dildar Hussain (hussain@kias.re.kr)

This work was supported in part by the Basic Science Research Program through the National Research Foundation of Korea (NRF), funded by the Ministry of Science and Information Communication Technology (MSICT) under Grant NRF-2017R1E1A1A01077717; in part by the Korea Institute for Advanced Study (KIAS) under Grant CG076601; and in part by the NRF grant funded by the MSICT through the Development Research Program under Grant NRF2022R1G1A101022611.

ABSTRACT Leukemia is one of the most terminal types of blood cancer, and many people suffer from it every year. White blood cells (WBCs) have a significant association with leukemia diagnosis. Research studies reported that leukemia brings changes in WBC count and morphology. WBC accurate segmentation enables to detect morphology and WBC count which consequently helps in the diagnosis and prognosis of leukemia. Manual WBC assessment methods are tedious, subjective, and less accurate. To overcome these problems, we propose a multi-scale information fusion network (MIF-Net) for WBC segmentation. MIF-Net is a shallow architecture with internal and external spatial information fusion mechanisms. In WBC images, the cytoplasm is with low contrast compared to the background, whereas nuclei shape can be complex with an indistinctive boundary for some cases, therefore accurate segmentation becomes challenging. Spatial features in the initial layers of the network include fine boundary information and MIF-Net splits and propagates this boundary information on multi-scale for external information fusion. Multi-scale information fusion in our network helps in preserving boundary information and contributes to segmentation performance improvement. MIF-Net also uses internal information fusion after intervals for feature empowerment in different stages of the network. We evaluated our network for four publicly available datasets and achieved state-of-the-art segmentation performance. In addition, the proposed architecture exhibits superior computational efficiency by using only 2.67 million trainable parameters.

INDEX TERMS Deep learning, computer-assisted diagnosis, leukemia diagnosis, WBC count, WBC segmentation.

I. INTRODUCTION

Blood is mainly composed of white blood cells (WBCs), red blood cells (RBCs), and platelets. WBCs in blood play a key role in fighting against infections, and detection of different diseases [1]. WBC count is also considered an important biomarker for the clinical diagnosis of many diseases. Leukemia is one of the fatal types of blood cancer and it occurs due to the replication of diseased WBCs. According to a study, every year approximately 300,000 new patients are diagnosed with leukemia [2]. Initially, leukemia suspected patients are advised for a complete blood test which includes WBC count. Moreover, the morphology of WBCs is also analyzed for confirmation of leukemia screening [3]. WBC count and morphology assessment are carried out manually which is tedious, time-consuming, error-prone, and subjective procedure. Hence, manual procedures are required to be replaced or assisted with artificial intelligence-based automated systems. Advances in computer-assisted diagnosis have a potential impact on the diagnostic industry [4].

The associate editor coordinating the review of this manuscript and approving it for publication was Zhen Ren.

Specifically, deep learning has played a vital role in various disease detection systems [5]. Computer-assisted diagnosis is the need of modern diagnostic systems. Leukemia diagnosis is significantly associated with WBC. Patients with leukemia exhibit changes in WBC count and morphology. Traditional diagnosis is based on manual assessment and analysis of WBCs. There is an improvement gap for accurate and early detection of leukemia which can be best filled with deep learning-based automatic and robust diagnosis frameworks. WBCs are normally classified into five main types; eosinophils, neutrophils, lymphocytes, basophils, and monocytes [4]. WBC segmentation is challenging because the cytoplasm is in low contrast with the background while the nucleus for some cases has an indistinctive boundary with a complex shape. Most of the existing WBC segmentation methods do not consider cytoplasm and nucleus joint segmentation. Moreover, some of the methods perform joint segmentation but their segmentation performance is not up to the mark. Lastly, many existing networks do not have a good computational efficiency therefore they require a large number of trainable parameters. In WBC segmentation, along with problems from the medical point of view, we have also discussed the challenges from a computer vision point of view in discussion section. To address these problems, we develop WBC segmentation network capable of performing joint segmentation for cytoplasm and nucleus with good computational efficiency. We used multi-scale information fusion for preserving and propagation of objects boundary information. We also used image information fusion for an improved feature extraction and enhanced learning. Information fusion from different stages of network helps in thorough learning of image features and results in accurate predictions. We improved segmentation performance using novel techniques without compromising the computational efficiency. We evaluated our architecture on four publicly available datasets and exhibited state-of-the-art segmentation performance. In Figure 1, sample images with their corresponding ground-truth images are shown. Leukemia brings changes to WBC count, and morphology [6] whereas morphological detection is mainly based on accurate boundary predictions for desired classes. In addition, there are a few statistical analyses based on the area of cytoplasm and nuclei which consequently aid in leukemia diagnosis.

Our main contribution to this study can be summarized as follows.

- We developed a novel network, namely multi-scale information fusion network (MIF-Net), for joint segmentation of cytoplasm and nucleus to highlight WBC morphology and count for aiding the leukemia diagnosis. MIF-Net possesses a shallow architecture with internal information fusion after intervals that improve the segmentation performance through feature empowerment.
- MIF-Net splits low-level multi-scale fine boundary information from the initial layer and propagates to deep stages of the network for external information fusion. It helps in accurate boundary predictions for both cytoplasm and nucleus. Proposed architecture is evaluated on four WBC publicly available datasets and achieved state-of-the-art segmentation performance. MIF-Net uses only 2.67 million trainable parameters, which confirms its promising computational efficiency.

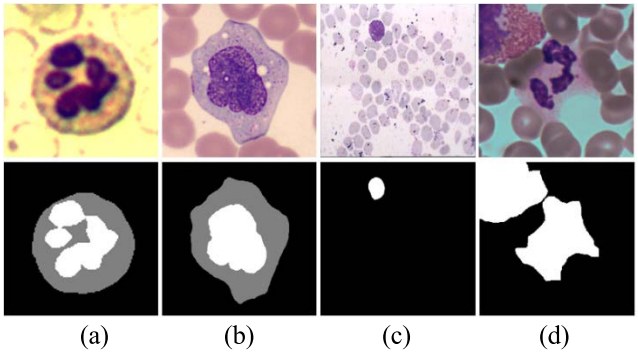

FIGURE 1. Example WBC images of datasets (row1) with ground-truth images (row2). (a) Dataset-1 (b) Dataset 2 (c) Dataset 3.

The remaining paper is organized as follows. Previous study related to WBC segmentation is discussed in Section II. Proposed method is explained in Section III. The experimental results along with implementation details are provided in Section IV. In the end, conclusion of this study is presented in Section V.

II. RELATED WORKS

WBC analysis is the topic of vast interest among medical experts because of its clinical significance in the diagnosis of many critical diseases. WBC segmentation methods can be mainly divided into two categories; WBC segmentation based on handcrafted-features and WBC segmentation based on deep-features.

A. WBC SEGMENTATION BASED ON HANDCRAFTED-FEATURES

Handcrafted-feature-based methods are generally based on conventional image processing schemes. In one of the methods, a color-band-thresholding scheme was employed for WBC segmentation, counting, and analysis [7]. This study concluded that color space components enable the computer-aided system to achieve the highest segmentation performance [7]. In addition, it also refers that nuclei-based detection exhibits better performance than cytoplasm-based detection for counting purposes [7]. However, the proposed assessment is limited to the same resolution and magnification factor, and tunning of a constant multiplier is required for other resolution and magnification factors [7]. Another study used hue, saturation, and value (HSV) components to improve the counting results in blood smear images [8]. According to this study [8], HSV components help in improving the accuracies using area features and eccentricity. Presented work eliminates the need for unnecessary preprocessing and provides a simple

and fast method for blood smear images analysis [8]. This method is evaluated using a few images [8]. Similarly, another method proposed adaptive histogram thresholding for leukocyte localization [9]. At first, nuclei is extracted followed by background removal using combination of image components and adaptive histogram thresholding. Later, the complete cell is extracted to obtain the cytoplasm region through subtraction operation [9]. This method is evaluated on a single dataset [9]. In [10], a clustering-based prediction method is proposed for decimating infected cells with non-infected cells. This method refers to a hybrid clustering approach in which a rough k-mean clustering is combined with rough soft covering clusters [10]. Method proposed in this study is capable of handling uncertainties by applying soft covering rough approximations [10]. Proposed method requires preprocessing and its processing time is expected to increase while working with multiple color images [10]. Subsequently, geometry and sparsity constraints are used to perform segmentation for nuclei and cytoplasm in leukocytes [11]. In this approach, accurate cell detection is achieved with the help of a fitting technique and effective information is preserved for better results [11]. This method was evaluated on datasets with single cell-based leukocyte images [11]. In another method, WBC assessment and segmentation are carried out by undergoing entropy-based procedures [12]. To improve the segmentation performance, a bi-level threshold is used in this approach [12]. Moreover, experiments are performed on a single famous leukocytes dataset for evaluation of their method [12]. In a study, the nucleus and cytoplasm of WBC are segmented using image texture and color-based enhancements [13]. In this method, cytoplasm highlighting, and elimination of undesired information are attained using enhancements and discrete wavelet transform [13]. This method requires contrast stretching as preprocessing to produce desired results [13]. In another method, leukocytes segmentation is performed using K-means clustering [14]. Initially, RGB image is converted and fed to K-mean clustering for extraction of nuclei. Finally, nuclei and background differences are taken from the main image to find cytoplasm [14]. Proposed method is evaluated on a single dataset [14].

B. WBC SEGMENTATION BASED ON DEEP-FEATURES

Deep learning has brought the conventional diagnostic industry to the verge of fast, automatic, and intelligent diagnostics. Deep learning-based segmentation approaches are famous because of their robustness and high segmentation performance. Deep-features-based methods are widely used in many computer-assisted diagnosis applications [4]. This study [4] refers to CNN-based algorithms that use transfer learning for WBC segmentation. However, this transfer learning-based approach had performance limitations especially for small cells [4]. In this study [15] some famous encoder-decoder-based segmentation architectures are employed for the segmentation of WBC. Proposed method employs VGG16 as an encoder and its features are used to improve the segmentation performance [15]. This method is evaluated on a single dataset for segmentation [15]. In this study, convolutional neural network (CNN) based on an encoder-decoder structure was used for WBC segmentation [16]. Multi-scale features were fed to the encoder whereas at the decoder-end, features were attained with the help of a context-aware feature map decoder to reconstruct the segmentation mask for predictions [16]. The proposed architecture is based on famous U-Net architecture [16]. Similarly, WBC multi-scale features were extracted with the help of a context-aware encoder in CNN [17]. A residual architecture performed features refinement and predictions were made with segmentation mask generation [17]. The network in the proposed method is based on famous U-Net architecture with the addition of a feature refinement module [17]. Subsequently in another method, initial segmentation is performed using an unsupervised technique [1]. In the first part, the foreground region of the image is extracted using K-means clustering. In the second part, support vector machine (SVM) is trained using the first part segmentation as labels. Finally, SVM provides the pixel-wise classification for further improvement in performance [1]. However, this method was tested on two datasets with no small-sized cells [1]. In a study, leukemia is diagnosed by initially performing segmentation and finally classifying the diseased and non-diseased cells [18]. In this method, fuzzy C means algorithm is combined with active contour output using a hybrid mutual information model for segmentation [18]. This framework needs preprocessing for predictions [18]. Subsequently, WBC segmentation is performed using multi-spectral imaging techniques [19]. SVM is directly applied on each pixel for pixel-wise segmentation whereas feature selection was conducted through sequential minimal optimization [19]. Feature vector is formed using the intensity of each pixel [19]. Similarly in [20], an algorithm for the recognition of five main types of WBCs is presented. Cytoplasm and nucleus segmentation is performed by using the snake algorithm and gram-Schmidt orthogonalization. After feature extraction, SVM and artificial neural network are employed for classification [20]. The proposed method has a limitation of generating multiple contours in case of multiple, separate, and apart nuclei regions in the same cell [20].

III. PROPOSED METHOD

A. PROPOSED METHOD OVERVIEW

The count and morphology of WBC are considered key biomarkers for the diagnosis of leukemia. Therefore, we develop a novel architecture for the segmentation of cytoplasm and nucleus in WBC microscopic images. The low contrast of cytoplasm and indistinctive boundary of nucleus for few images can make the WBC segmentation challenging. We develop a multi-scale information fusion-based architecture to deal with these challenges. Extracted features in initial layers of any network carry potential

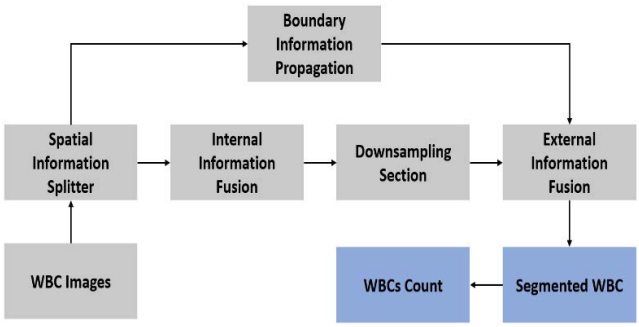

FIGURE 2. Overview of proposed multi-scale information fusion-based cytoplasm and nuclei segmentation network in white blood cells (WBCs) images for aiding the leukemia diagnosis.

low-level spatial information. Overview of the proposed framework is shown in Figure 2. WBC images are provided to spatial information splitter as input. This spatial information includes fine boundary information which is splitted in multi-scale using spatial information splitter. Fine boundary information is propagated to the advance layers of the network for information fusion. In the external information fusion section, boundary information is fused with downsampled spatial information. External information fusion significantly helps in boundary predictions for the cytoplasm and nucleus. Moreover, splitter also transfers spatial information for internal fusion. Internal information fusion ensures feature empowerment across the network. Internal fused information is periodically downsampled and finally after a few layers of operations it is also fused with external information fusion. In the end, prediction masks are generated in accordance with fused features. Our network provides segmented cytoplasm and nucleus along with WBC count as output which can aid in the diagnosis and prognosis of leukemia.

B. CYTOPLASM AND NUCLEUS SEGMENTATION USING MIF-NET

WBC microscopic images are usually different in shape, stain condition, and size which makes their segmentation challenging. We developed a multi-scale information fusion-based network that is capable of delivering better segmentation performance even in challenging conditions. The network architecture of proposed MIF-Net is shown in Figure 3. Spatial information of input image is extracted using image input layer. This spatial information is splitted through spatial information splitter which is based on a convolution layer. Spatial information splitter splits the spatial information in three different scales using strided convolution layers. These multi-scale image features significantly help in segmentation performance improvement. U-Net [21] and SegNet [22] are famous encoder-decoder-based segmentation architectures. In encoder-decoder structures, pooling layers and un-pooling layers are used for downsampling and upsampling of spatial information, respectively. Pooling and un-pooling layers cause information loss along with their normal operation [23]. This information loss is more crucial at the decoder-end because after decoding prediction masks are generated. To cater this problem, MIF-Net uses a shallow architecture and we employ transpose convolution in place of un-pooling layers. Similarly, we use strided convolution in place of pooling layers for multi-scale information downsampling, and propagation. Both transpose and strided convolution layers are learnable layers and help the network in optimum learning. In addition, MIF-Net presents a unique internal and external information fusion concept. Initial layers of the network possess fine boundary information of the objects and we propagated this boundary information in the boundary information propagation (BIP) section. BIP uses strided convolution for multi-scale propagation of spatial information. Three strided convolution layers with the corresponding stride (S-1/S-2/S-3) took part in multi-scale information dissemination and later this information is fused with spatial information in external information fusion blocks. As shown in Figure 3, we used two categories of fusions; External information fusion (EIF) and internal information fusion (IIF). In EIF, all three skip connections are originated from the encoder's first layer (splitter), bypassing the remaining encoder layers and passing through BIP, which are terminated in the decoder. Therefore, all the fusions in decoder getting external inputs from the encoder are named EIF. In the proposed architecture, three EIFs are employed for multi-scale external information fusion. In all IIF, skip connections are originated from the encoder's preceding convolution layer and are terminated in the subsequent convolution layer of encoder. Hence, all the fusions in encoder getting internal input from encoder are named IIF. In the proposed network, four IIF are employed for spatial feature empowerment after intervals. Three EIF blocks, namely EIF-1, EIF-2, and EIF-3 are used for external information fusion between boundary information and downsampled spatial information. Generally, all network layers cause some feature degradation along with their normal operation. MIF-Net developed an internal information fusion scheme to compensate for this feature degradation problem. MIF-Net design contains four IIF blocks; namely IIF-1, IIF-2, IIF-3 and IIF-4 which are employed for feature empowerment. S-1 shows the strided convolution with stride 1 and it takes the input from splitter and provides the output to EIF-3. Similarly, S-2 refers to strided convolution with stride 2 and it also takes the input from splitter, reduces the feature map size with a factor of 2 (half), and its output is fed to EIF-2 for information fusion. S-4 shows the strided convolution with stride 4. S-4 also takes input from splitter; reduces the feature map size with a factor of 4 (quarter) and its output is fused at EIF-1.

In Figure 4, we presented both external and internal fusion process interpretation for a detailed explanation. As shown in Figure 4, *S_conv_i* refers to the strided convolution which is itself the part of BIP. Features being input to *S_conv_i* (BIP) are originated from spatial information splitter. Two convolution layers conv i and conv j provides spatial features of $I_a$and I_b, respectively. The addition symbol given at the left side of Figure 4 represents IIF and both spatial features,

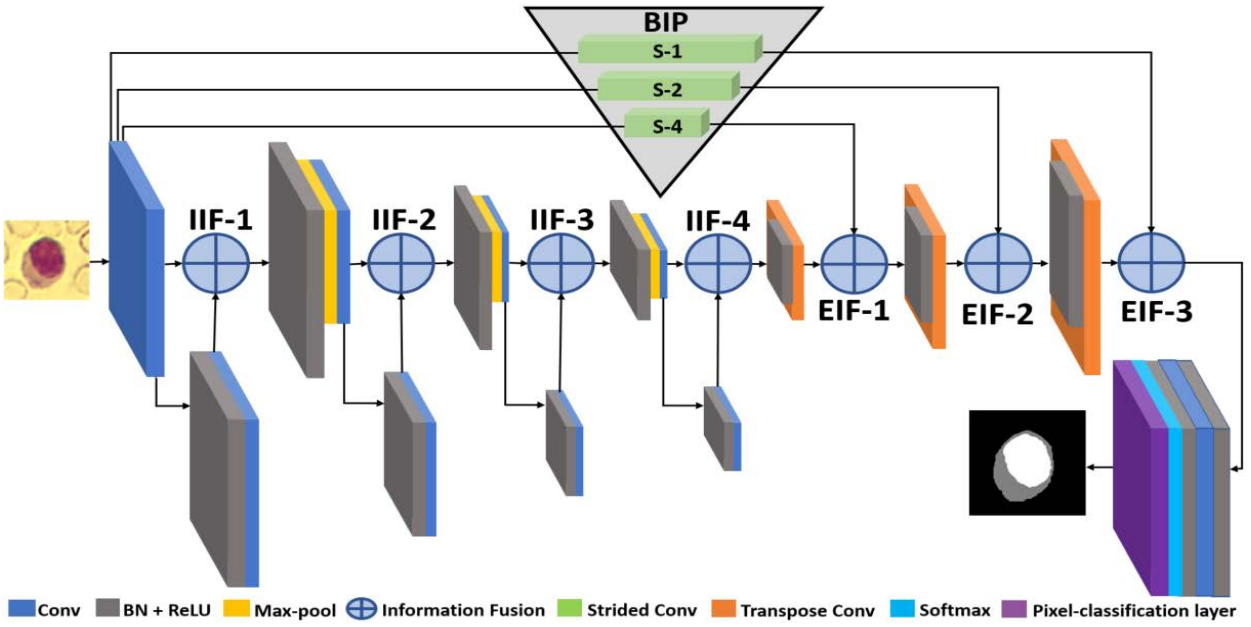

FIGURE 3. MIF-Net architecture. (IIF: internal information fusion; EIF: External information fusion; BIP: Boundary information propagation; S: Stride; Conv: Convolution layer; Max-pool: Max-pooling layer; ReLU: Rectified linear unit layer; Transpose Conv: Transpose convolution layer; BN: Batch normalization layer; PCL: Pixel classification layer; Strided Conv: Strided convolution layer; S-1: Stride-1; S-2: Stride-2; S-4: Stride-4).

$I_a$and I_b, are fused producing internally fused feature IF_m at the output.

$$IF_m = I_a + I_b \tag{1}$$

Transpose convolution (T_conv_j) upsamples the internally fused feature and provides IF'_m at the output. Splitted spatial boundary information is fed to strided convolution (S_conv_i) for information propagation in designated scale and it provides spatial boundary information (SB_n) at its output. This SB_n and IF'_m are fused and provides external fused spatial boundary information (EF_p) as given in mathematical expression below

$$EF_p = IF'_m + SB_n \tag{2}$$

This external fused boundary information is further processed through batch normalization (BN_i) and rectified linear unit (ReLU) and changes in spatial information is represented with Δ. The final output is fed to the next external information fusion block.

$$\Delta EF_p = \Delta(IF'_m + SB_n) \tag{3}$$

Loss function in any deep learning-based convolutional neural network guides the network for optimal learning. In the proposed architecture binary cross-entropy loss is employed to lead the training process. MIF-Net layer level configurational detail is presented in Table 1.

C. MIF-NET ARCHITECTURE COMPARATIVE DETAILS

MIF-Net architecture is developed from scratch, and it is not based on any other network. The initial layers of the network contain low-level spatial information. This low-level spatial information from the initial layer is splitted into four paths for

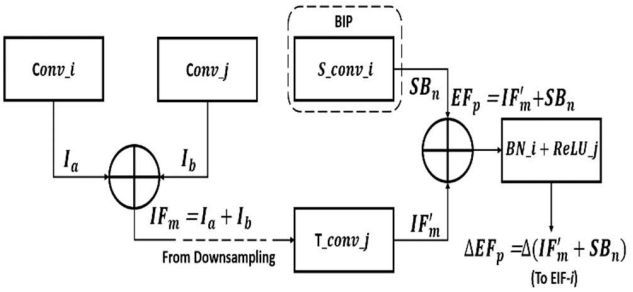

FIGURE 4. Schematic diagram of the MIF-Net showing internal and external spatial information fusion. Whereas, symbol at the left side and right side of the diagram represents IIF and EIF, respectively.

external and internal information fusions. Splitter is based on a convolution layer followed by BN and ReLU layers. The splitting of spatial information is shown in Figure 5. Three strided convolution layers with strides 1, 2, and 3 change the features to multi-scale according to their stride values. Feature map size at splitter (Conv1_1) is $300 \times 300 \times 64$ and after strided-conv (S-2) feature map size becomes $150 \times 150 \times 64$ because of stride value of 2. Similarly, after strided-conv (S-4) feature map size is downsampled to $75 \times 75 \times 128$ with increased channels. Lastly, strided-conv (S-1) retains the feature map size ($300 \times 300 \times 32$) with decreased number of channels and applies the convolution operation for the last external information fusion. All this multi-scale information from strided convolution layers subsequently undergoes EIF. In MIF-Net, IIF ensures feature empowerment after intervals whereas EIF helps in improved boundary predictions for cytoplasm and nucleus.

Multi-scale information fusion is being widely used in different deep learning-based applications [45],[46]. In [45],

TABLE 1. MIF-net configurational description.

Layer Name	No. of filters	No. of parameters	Output (W × H × C)
Conv1_1+ReLU1_1	64	1792	300×300×64
BN_Conv1_1	-	128	300×300×64
Conv1_2+ReLU1_2	64	36,928	300×300×64
BN_Conv1_2	-	128	300×300×64
Conv2_1+ReLU2_1	128	73856	150×150×128
BN_Conv2_2	-	256	150×150×128
Conv2_2+ReLU2_2	128	147,584	150×150×128
BN_Conv2_2	-	256	150×150×128
Conv3_1+ReLU3_1	256	295,168	75×75×256
BN_Conv3_1	-	512	75×75×256
Conv3_2+ReLU3_2	256	590,080	75×75×256
BN_Conv3_2	-	512	75×75×256
Conv4_1+ReLU4_1	256	590,080	38×38×256
BN_Conv4_1	-	512	38×38×256
Conv4_2+ReLU4_2	256	590,080	38×38×256
BN_Conv4_2	-	512	38×38×256
S_Conv_1	128	8320	75×75×128
T_conv1+ReLU-1t	128	295,040	75×75×128
BN_1t	-	256	75×75×128
S_Conv_2	64	4160	150×150×64
T_conv2+ReLU-2t	64	32,832	150×150×64
BN_2t	-	128	150×150×64
S_Conv_3	32	2080	300×300×32
T_conv3+ReLU-3t	32	8,224	300×300×32
BN_3t	-	64	300×300×32
Conv5+ReLU5	3	99	300×300×3
BN_Conv5	-	6	300×300×3
Total number of parameters:		2,679,593	

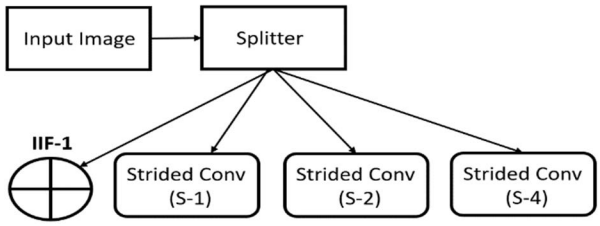

FIGURE 5. Spatial information splitting diagram. (Strided Conv: Strided convolution layer; S-1: Stride-1; S-2: Stride-2; S-4: Stride-4)

a scale estimation network (SENet) with head detection network is presented for person localization. SENet employs ResNet-101 as the backbone to address the problem of vanishing gradient. Similarly, in [46] multi-scale object proposal method followed by multi-class object classification is proposed. In this method, a feature pyramid network (FPN) is employed for multi-scale feature maps to be converted into object proposals. FPN is used with the backbone of ResNet. MIF-Net is an entirely different architecture compared with [45] and [46], some of the major differences are highlighted in Table 2. In MIF-Net, a maximum of 256 channels are used which results in a small number of parameters requirement. Subsequently, only three down-sampling operations are performed in MIF-Net to keep the final feature map size sufficiently large for avoiding minor information loss. Unlike [45], [46], the proposed method uses a total of 7 fusion operations including EIF and IIF. In the proposed method, spatial information is splitted from the initial layer. Multi-scale information in MIF-Net is attained using strided convolution with different stride values. MIF-Net architecture is a computationally efficient architecture, and it requires only 2.67 million trainable parameters.

TABLE 2. MIF-NET key Differences with SENet[45] and FPN-based method [46].

Models	MIF-Net	SENet	FPN-based
Number of max channels	256	2048	512
Number of downsampling operations	3	5	5
Maximum stride value used	4	2	2
Number of convolution layers in each stage (excluding upconvolution and first stage)	2	3	4
Fusion points	7	1	3
Multi-scale architecture base	Developed from scratch	Based on ResNet-101	FPN+ResNet
Spatial information splitting from the initial layer	YES	NO	NO
Architecture type	Segmentation	Region-prposal-based detection	Region-prposal-based detection
Number of parameters	2.67 M	44.5 M (ResNet-101)	-

IV. DATASET DESCRIPTION AND TRAINING

A. DESCRIPTION OF EXPERIMENTAL SETUP AND DATABASES

We performed experiments on four publicly available datasets to evaluate the proposed framework. Jianxi Tecom Science corporation of China provided Dataset-1 [1]. Dataset-1 has 300 images with 120 × 120 dimensions. It contains 48 monocytes, 176 neutrophils, 1 basophil, 22 eosinophils, and 53 lymphocytes. Similarly, Dataset 2 [1] has a total of 100 images with 300 × 300 dimensions. It contains 18 monocytes, 30 neutrophils 3 basophils, 12 eosinophils, and 37 lymphocytes. Dataset 3 [20] consists of 242 images with 712 × 568 dimensions. It has 48 monocytes, 50 neutrophils, 53 basophils, 39 eosinophils, and 52 lymphocytes. Dataset 2, and 3 employed a standard staining condition whereas Dataset-1 used a rapid staining condition. Sample images for all four datasets are already shown in Figure 1. Dataset 4 (BCISC) [49] has a total of 268 sub-images with size 256 × 256 pixels and its collection is supported by third people's hospital of Fujian province.

MIF-Net is developed, trained, and evaluated using MATLAB R2020a. We performed experiments using a computer having Intel®Core^{TM}i7 3770 with 28 GB of RAM, 3.5 GHz CPU, and NVIDIA GeForce GTX 1070 GPU.

B. MIF-NET TRAINING

Neural networks require extensive annotated data for the optimal training of the network. Annotated medical images data is usually insufficient for training. Therefore, we perform augmentation of training data to artificially create the training database. In augmentation, we logically perform different morphological, geometric, and arithmetic operations. In our data preparation, we used vertical and horizontal flipping along with different translation and cropping schemes for data augmentation. We used the original image size for Dataset 2 experiments whereas Dataset-1 and dataset 3 were resized to 300×300 and 712×568, respectively. Same data splitting criteria are followed as given in [16]. Hence, 70% of images are randomly selected for training while 30% of images are randomly selected as testing whereas 10% of the training split is used for validation to avoid overfitting. We trained our network from scratch; we did not use any pre-trained network or weights migration for our model training. Adaptive moment estimation (Adam) is employed as an optimizer to optimize the adaptive learning process [24]. Adam optimizer is famous for its fast convergence with limited memory requirements using a first-order gradient [24]. Class labels identifiers based on corresponding ground-truth images are assigned before starting the training process. An initial learning rate of 0.001, L2 regularization of 0.0005, and a square gradient decay factor of 0.95 were set as initial training hyperparameters. Overall optimization is attained using Adam optimizer. Validation is used to ensure that network is not overfitted with training data. A stopping criterion based on validation accuracy with a stopping threshold value of 20 is adopted. If the validation accuracy does not increase for 20 consecutive iterations training stops and network with optimized hyperparameters is saved. with threshold value of 20 is set to stop and save the network with optimized hyperparameters. avoid the overfitting The training loss and accuracy plots are shown in Figure 6(a), 6(b), and 6(c) represents that the training accuracy is approaching to approximately 100% with decaying loss for all datasets. Similarly, validation accuracy and loss plots shown in Figure 6(d)-(f) represent that our model is not overfitted with training data.

C. EVALUATION METRICS

We evaluated the proposed network on four publicly available datasets and compared our results with existing state-of-the-art results. We presented both visual and numeric results for comparative evaluations. We performed segmentation for cytoplasm and nucleus for Dataset-1 and 2 whereas Dataset 3 has only cytoplasm annotations (for basophils) therefore we performed segmentation for cytoplasm only. Evaluation metrics used for MIF-Net includes precision (PRE) [25], misclassification error (ME) [26], the dice coefficient (DI) [27], mean intersection over union (mIoU) [28], false-positive rate (FPR) [29], and false-negative rate (FNR) [11]. Mathematical expressions of evaluation measures are shown in equations (4)-(9).

$$\text{Precision} = \frac{\left|W_f \cap P_f\right|}{\left|P_f\right|} \tag{4}$$

$$\text{DI} = \frac{2\left|W_f \cap P_f\right|}{\left|W_f\right| + \left|P_f\right|} \tag{5}$$

$$\text{mIoU} = \frac{1}{2}\left(\frac{|W_b \cap P_b|}{|W_b \cup P_b|} + \frac{\left|W_f \cap P_f\right|}{\left|W_f \cup P_f\right|}\right) \tag{6}$$

$$\text{ME} = 1 - \frac{|W_b \cap P_b| + \left|W_f \cap P_f\right|}{\left|W_f\right| + |W_b|} \tag{7}$$

$$\text{FPR} = \frac{\left|W_b \cap P_f\right|}{|W_b|} \tag{8}$$

$$\text{FNR} = \frac{\left|W_f \cap P_b\right|}{\left|W_f\right|} \tag{9}$$

W_f represent the desired region whereas W_b represents the undesired region, in WBC ground-truth image. Likewise, P_f refers to desired predicted segmentation result whereas $P_b$refers to undesired predicted segmentation results. Same evaluations are also presented in terms of true positive (TP), false-positive (FP), and false-negative (FN) using different colors for visual interpretation of qualitative results. A higher DI and mIoU refers to a better segmentation performance likewise, a lower ME, FPR, FNR score also represents a better segmentation performance.

V. EXPERIMENTAL RESULTS

We present both numeric and visual results of MIF-Net evaluation for a comprehensive assessment.

A. MIF-NET SEGMENTATION RESULTS ON DATASET-1

Experiments were performed on Dataset-1 for the joint segmentation of cytoplasm and nucleus. Dataset-1 possesses a rapid stain condition; consequently, the contrast of cytoplasm with background is low which makes the segmentation challenging. As shown in Figure 8, nucleus boundary is indistinctive in a few cases, hence accurate boundary prediction becomes intriguing for such WBC nucleus. Multi-scale information fusion mechanism in MIF-Net helps the network in preserving boundary information. Despite challenges, MIF-Net manages to exhibit state-of-the-art segmentation performance using its effective design. Dataset-1 good segmentation results are shown in Figure 7 whereas some poor segmentation images are provided in Figure 8. poor segmentation results are because of staining conditions, contrast limitation, and indistinctive boundary of objects.

Dataset-1 numerical results comparison with state-of-the-art methods for cytoplasm and nucleus is presented in Table 3 and 4, respectively. Numerical results also confirm the superior segmentation performance of the proposed network.

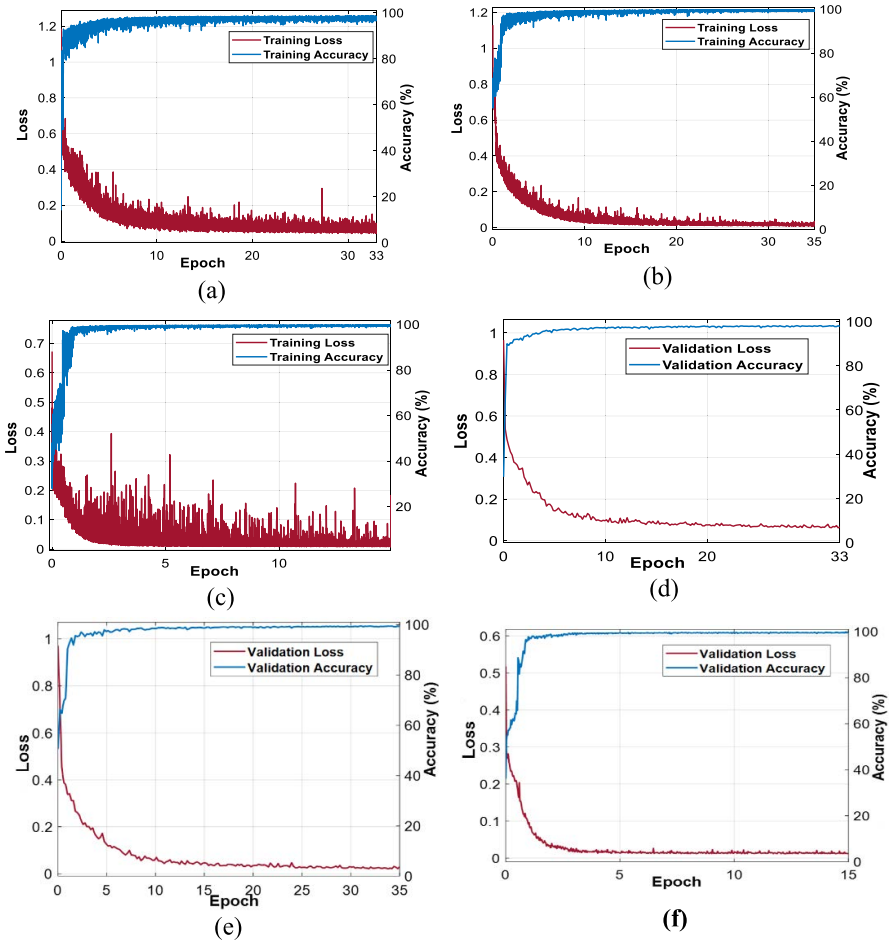

FIGURE 6. MIF-Net training accuracy and loss curves for (a) Dataset-1, (b) Dataset 2, and (c) Dataset 3. Validation accuracy and loss curves with MIF-Net for (d) Dataset-1 and (e) Dataset 2, and (f) Dataset 3.

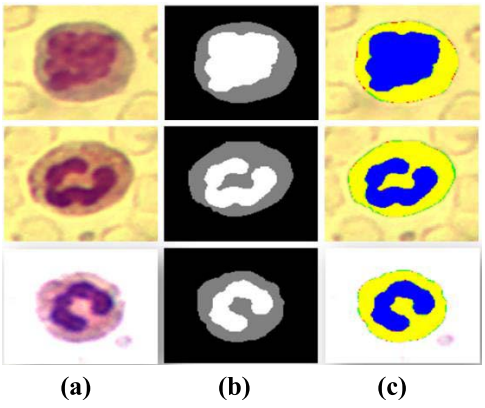

FIGURE 7. Good WBC segmentation visual results for cytoplasm and nuclei on Dataset-1. (a) Original image, (b) ground-truth image, and (c) segmented images obtained using MIF-Net. (TP pixels for cytoplasm and nucleus segmentation are denoted by yellow and blue color, respectively. Moreover, FP pixels are represented by green and FN pixels are represented by red).

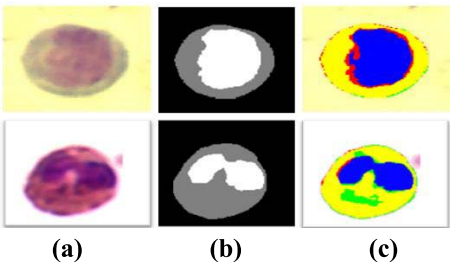

FIGURE 8. Poor WBC segmentation visual results for cytoplasm and nuclei on Dataset-1. (a) Original image, (b) ground-truth image, and (c) segmented images obtained using MIF-Net. (TP pixels for cytoplasm and nuclei segmentation are denoted by yellow and blue color, respectively. Moreover, FP pixels are represented by green and FN pixels are represented by red).

B. MIF-NET SEGMENTATION RESULTS ON DATASET 2

Experiments were performed to evaluate the proposed method on Dataset 2 for the joint segmentation of cytoplasm and nucleus. Dataset 2 images also have low contrast between cytoplasm and background. It makes the learning process challenging for the network. However, MIF-Net still manages outperforming results using its information fusion-based advance design. Visual results for good segmentation and poor segmentation of cytoplasm and nucleus are shown in Figures 9 and 10, respectively. Poor segmentation results are because of indistinctive boundaries in the cells. In the second

TABLE 3. Comparison of numerical results with state-of-the-art methods for cytoplasm segmentation using MIF-net on dataset-1. "- " refers to results unreported (unit: %).

Methods	PRC	DC	mIoU	ME	FNR	FPR
Zheng *et al.* [43]	86.53	92.5	-	5.2	0.03	7.8
Zhou *et al.* [29]	88.71	90.34	-	6.3	5.4	6.9
U-Net [21]	97.43	97.32	-	1.59	2.7	1.18
Chen *et al.* [16]	98.03	97.37	-	1.58	3.23	0.96
MIF-Net (proposed)	98.98	98.93	97.91	0.66	1.05	0.52

TABLE 4. Comparison of numerical results with state-of-the-art methods for nucleus segmentation using MIF-net on dataset-1. "- " refers to results unreported (unit: %).

Methods	PRC	DC	mIoU	ME	FNR	FPR
Sarrafzadeh *et al.*[14]	-	70.88	-	-	-	-
Vincent *et al*.[42]	-	48.33	-	-	-	-
Vogado *et al*. [39]	-	87.68	-	-	-	-
Makem *et al.*[40]	91.01	90.79	-	2.7	-	-
Banik *et al.*[41]	87.63	91.0	-	-	-	-
MIF-Net (proposed)	93.81	95.84	92.18	0.997	1.76	0.85

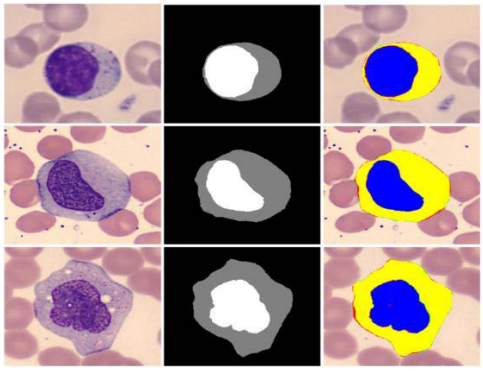

FIGURE 9. Good WBC segmentation visual results for cytoplasm and nuclei on Dataset 2. (a) Original image, (b) ground-truth image, and (c) segmented images obtained using MIF-Net. (TP pixels for cytoplasm and nucleus segmentation are denoted by yellow and blue color, respectively. Moreover, FP pixels are represented by green and FN pixels are represented by red).

TABLE 5. Comparison of numerical results with state-of-the-art methods for cytoplasm segmentation using MIF-net on dataset 2. "- " refers to results unreported (unit: %).

Methods	PRC	DC	mIoU	ME	FNR	FPR
Zheng *et al.* [43]	53.61	66.93	-	25.36	0.42	32.6
Zhou *et al.* [29]	73.94	76.05	-	13.25	10.3	13.6
U-Net [21]	92.76	94.98	-	2.32	2.4	2.15
Chen *et al.* [16]	94.2	96.18	-	1.17	1.6	1.8
MIF-Net (proposed)	99.51	98.38	96.82	0.711	2.69	0.15

row of Figure 10, poor segmentation results can be attributed to granules in the nucleus.

Numerical results comparison with state-of-the-art methods is also presented in Tables 5 and 6 for cytoplasm and nucleus, respectively. MIF-Net exhibits better segmentation performance compared with other methods.

C. MIF-NET SEGMENTATION RESULTS ON DATASET 3

Proposed architecture is further evaluated on Dataset 3 to check its effectiveness. Dataset 3 contains images with

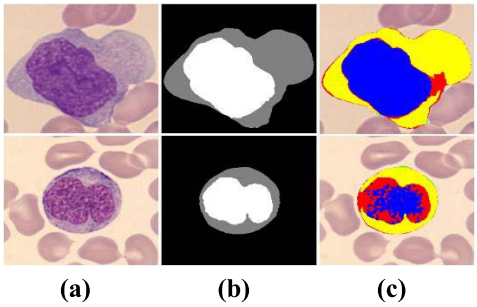

FIGURE 10. Poor WBC segmentation visual results for cytoplasm and nuclei on Dataset 2. (a) Original image, (b) ground-truth image, and (c) segmented images obtained using MIF-Net. (TP pixels for cytoplasm and nucleus segmentation are denoted by yellow and blue color, respectively. Moreover, FP pixels are represented by green and FN pixels are represented by red).

TABLE 6. Comparison of numerical results with state-of-the-art methods for nucleus segmentation using MIF-net on dataset 2. "- " refers to result unreported (unit: %).

Methods	PRC	DC	mIoU	ME	FNR	FPR
Sarrafzadeh et al.[14]	-	92.12	-	-	-	-
Vincent et al.[42]	-	90.49	-	-	-	-
Vogado et al. [39]	-	93.22	-	-	-	-
Makem et al.[40]	97.37	97.06	-	0.62	-	-
Banik et al.[41]	91.75	94.0	-	-	-	-
MIF-Net (proposed)	99.27	97.53	95.66	0.511	3.62	0.063

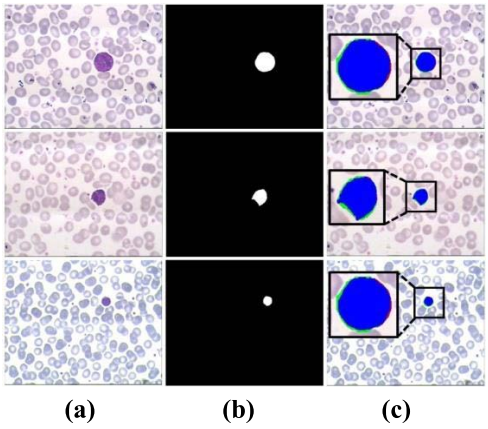

FIGURE 11. Good WBC segmentation visual results for cytoplasm on Dataset 3. (a) Original image, (b) ground-truth image, and (c) segmented images obtained using MIF-Net. (TP, FP, and FN pixels for cytoplasm are represented by blue, green, and red color, respectively).

small-sized cells and some images are containing multiple cells in the same image. MIF-Net still delivers outperforming segmentation results for pixel-wise predictions. Good and poor segmentation visual results are shown in Figures 11 and 12, respectively. Poor segmentation results are because of small-sized WBCs available in the dataset.

Subsequently, numerical results comparison with state-of-the-art segmentation methods is given in Table 7. This comparison also validates the effectiveness of MIF-Net for WBC segmentation.

D. MIF-NET SEGMENTATION RESULTS ON DATASET 4

MIF-Net is further evaluated on Dataset 4 to confirm the effectiveness of the proposed method. This dataset has a

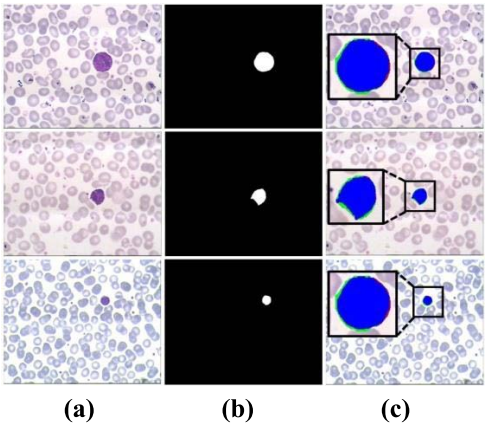

FIGURE 12. Poor WBC segmentation visual results for cytoplasm on Dataset 3. (a) Original image, (b) ground-truth image, and (c) segmented images obtained using MIF-Net. (TP, FP, and FN pixels for cytoplasm are represented by blue, green, and red color, respectively).

TABLE 7. Comparison of numerical results with state-of-the-art methods for cytoplasm segmentation using MIF-net on dataset 3. "- " refers to results unreported (unit: %).

Methods	PRC	DC	mIoU	ME	FNR	FPR
Tareef *et al.* [13]	-	88.7	-	-	-	-
Manasi *et al.* [12]	95.51	90.49	86.44	-	-	-
U-Net [21]	91.09	94.04	91.18	-	-	-
SegNet [22]	91.59	94.30	91.20	-	-	-
VGG-UNet [15]	91.56	94.40	91.51	-	-	-
MIF-Net (proposed)	93.83	95.2	91.16	0.08	2.87	0.06

TABLE 8. Comparison of numerical results with state-of-the-art methods for cytoplasm segmentation using MIF-net on dataset 4. "- " refers to results unreported (unit: %).

Methods	PRC	DC	mIoU	ME	FNR	FPR
Watershed [47]	97.40	83.18	82.26	5.0	26.1	0.4
FCN [48]	94.75	95.82	95.20	1.37	2.89	1.07
U-Net [21]	93.0	95.08	94.42	1.66	2.4	1.47
LeukocyteMask (Aug-ET) [49]	98.94	97.83	96.47	1.10	3.54	0.19
MIF-Net (proposed)	98.45	97.95	96.41	0.006	0.19	0.03

few cases having multiple cells in the same image. Some of the cells are quite close to each other. Qualitative results presented in Figure 13 confirm that the proposed method exhibit good segmentation performance. More specifically, in Figure 13 (rows 4 and 5), some cells in the same image are quite close to each other, nonetheless, MIF-Net provides good segmentation for such challenging cases as well.

Quantitative results comparison with state-of-the-art methods is presented in Table 8. Quantitative results in Table 8 includes multiple close cells cases as shown in Figure 13 (rows 4 and 5). It also confirms the outperforming segmentation accuracies of the proposed method requiring only 2.6 million trainable parameters.

E. DISCUSSION

This study proposes a comprehensive framework for joint segmentation of cytoplasm and nucleus from WBC images.

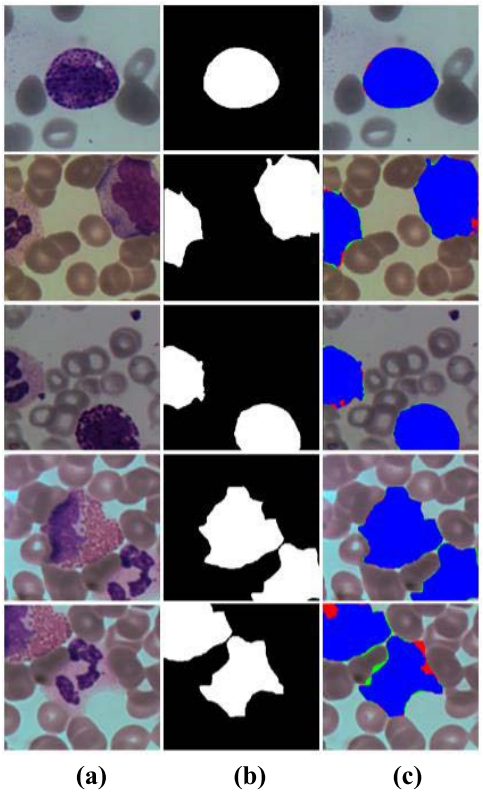

FIGURE 13. WBC segmentation visual results for cytoplasm on Dataset 4. (a) Original image, (b) ground-truth image, and (c) segmented images obtained using MIF-Net. (TP, FP, and FN pixels for cytoplasm are represented by blue, green, and red color, respectively).

It is evident from clinical literature that leukemia brings changes in morphology and count of WBCs. Accurate segmentation of WBC leads to exhibiting accurate morphology and provides the exact area of the nucleus and cytoplasm. Therefore, the proposed method can aid in the diagnosis and prognosis of leukemia and other related diseases. WBCs are different in shape, size, and morphology which makes the segmentation task challenging. MIF-Net still manages to exhibit good performance by transferring fine boundary information, and multi-scale information fusion using its effective architecture. To confirm it we perform cross-dataset evaluation between multiclass datasets; Dataset-1 and Dataset 2. Results of cross-dataset segmentation evaluation for Dataset-1 and 2 are provided in Tables 9 and 10, respectively. Dataset-1 is evaluated using a trained network with Dataset 2 whereas Dataset 2 evaluation is carried out using a trained network with Dataset-1. The main reasons for underperformance, in cross-dataset evaluation, are possibly the stain and RBCs difference. Dataset-1 uses a rapid staining condition whereas Dataset 2 has a standard staining process. Moreover, Dataset 2 has several adjacent solid-shaped RBCs which influence the network predictions while cross-dataset evaluation. Despite dealing with major changes, MIF-Net still manages to provide a better cross-dataset performance which confirms the generalizability of the proposed method.

TABLE 9. Segmentation results of dataset-1 trained on dataset 2 using MIF-net for cross-dataset evaluation. (unit: %).

Methods	PRC	DC	mIoU	ME	FNR	FPR
MIF-Net (Cytoplasm)	90.18	92.89	87.50	4.78	3.50	5.28
MIF-Net (Nucleus)	92.01	89.11	83.01	3.81	5.94	2.41

TABLE 10. Segmentation results of dataset 2 trained ondataset-1 using MIF-net for cross-dataset evaluation. (unit: %).

Methods	PRC	DC	mIoU	ME	FNR	FPR
MIF-Net (Cytoplasm)	85.53	91.89	85.34	3.74	1.94	4.43
MIF-Net (Nucleus)	85.46	91.69	85.29	1.89	0.45	2.10

TABLE 11. Ablation studies for comparison of numerical results using MIF-net (proposed) and MIF-Net (pooling) for cytoplasm segmentation (unit: %).

Dataset	Method	PRC	DC	mIoU	ME	FNR	FPR
Dataset-1	MIF-Net (pooling)	98.14	97.83	95.81	1.44	2.36	0.99
	MIF-Net (Proposed)	98.98	98.93	97.91	0.66	1.05	0.52
Dataset 2	MIF-Net (pooling)	98.95	97.47	95.13	1.01	3.87	0.26
	MIF-Net (Proposed)	99.51	98.38	96.82	0.711	2.69	0.15
Dataset 3	MIF-Net (pooling)	90.66	94.39	89.81	0.11	1.08	0.11
	MIF-Net (Proposed)	93.83	95.20	91.16	0.08	2.87	0.06

TABLE 12. Ablation studies for comparison of numerical results using MIF-net (proposed) and MIF-net (pooling) for nucleus segmentation (unit: %).

Dataset	Method	PRC	DC	mIoU	ME	FNR	FPR
Dataset-1	MIF-Net (pooling)	90.62	91.56	85.51	2.22	5.23	1.72
	MIF-Net (Proposed)	93.81	95.84	92.18	0.997	1.76	0.85
Dataset 2	MIF-Net (pooling)	97.51	96.58	94.69	0.60	3.30	0.22
	MIF-Net (Proposed)	99.27	97.53	95.66	0.511	3.62	0.063

1) ABLATION STUDY

In CNN's, pooling layers are traditionally employed for downsampling purposes. However, many studies reported that pooling layers also cause information loss and features degradation [23]. Therefore, we replaced pooling layers with strided convolutional layers to minimize spatial information loss and thereby to achieve enhanced performance. As presented in Table 1, convolution layers are using a maximum of 256 channels, therefore, the number of trainable parameters required by each convolution layer is not much high, and the proposed network is able to outperform using only 2.67 million parameters. In the trade-off between segmentation performance and trainable parameters, we preferred segmentation performance as the total number of trainable parameters was not too high. A large stride is preferred for better performance in CNNs [44], MIF-Net also uses large stride values for multi-scale features propagation as presented in Figure 3. Ablation studies are presented to compare the segmentation results of the proposed MIF-Net using strided convolution (proposed) with MIF-Net using pooling layers. Segmentation performance difference for cytoplasm and nucleus is presented in Tables 11 and 12, respectively. Ablation studies confirm that the replacement of pooling layers with strided convolution layers is useful to achieve better segmentation performance.

2) MIF-NET TECHNICAL CONTRIBUTION

MIF-Net is developed for the joint segmentation of cytoplasm and nuclei from WBCs microscopic images. Initial layers of a CNN contain valuable fine boundary information of the objects. As shown in Figure 3, we split this boundary information in multi-scale using strided convolution layers with different strides. BIP in MIF-Net employs strided-convolution in place of pooling layers to increase the learnability of BIP. It is evident from the ablation study presented in Tables 11 and 12, that the replacement of pooling layers with strided convolution enables the network to achieve significant performance differences. This multi-scale information is fused at different stages of the network for improved boundary predictions. Subsequently, we employed IIF after intervals for reducing the spatial loss and thereby ensuring the features empowerment. Information fusions used in our architecture are based on residual connectivity. To the best of our knowledge, this is the first residual connectivity-based architecture using both internal and external fusions simultaneously for WBCs joint segmentation. The proposed method exhibited outperforming results with a promising computational efficiency.

3) CHALLENGES IN WBC SEGMENTATION

In WBCs segmentation, along with problems from medical point of view, there are number of issues and complexities from the computer vision perspective as well. Some of the challenges associated with WBCs segmentation are exhibited in Figure 14. WBCs can have equal or even smaller sizes compared to adjacent erythrocytes which can make its segmentation challenging (row 2, Figure 14). In some cases, the nucleus indistinctive boundary and irregular shape can also become a problem for accurate segmentation (row 5, Figure 14). Similarly, cytoplasmic boundary predictions are also challenging in the case of several adjacent RBCs with cell (row 4, Figure 14). Some of the images have adjacent cut-cells which can also mislead the network for false prediction (row 3, Figure 14). In our case, cut-cells could not hit the accuracy of the network for WBC segmentation or count. In the last row of Figure 14, a sample WBC image with nucleated RBC (NRBC) from Dataset 2 is shown. Since NRBC also has a nucleus therefore its segmentation becomes challenging. As evident from Figure 14 (row 6), the proposed method managed to deliver promising segmentation performance even with NRBCs. Quantitative results for Dataset 2 in Tables 5 and 6 are computed with inclusion of NRBC. However, NRBC cases are rare in all four datasets of this study. Therefore, we intend to work on WBC segmentation with the majority of NRBC cases in the future. Many images have WBCs adjacent to RBCs and interestingly it also could not mislead the proposed network (row 4, Figure 14). Likewise, some images have multiple cells in a single image nevertheless MIF-Net provides a high segmentation performance with accurate WBCs count (row 1, Figure 14). However, the segmentation-based method

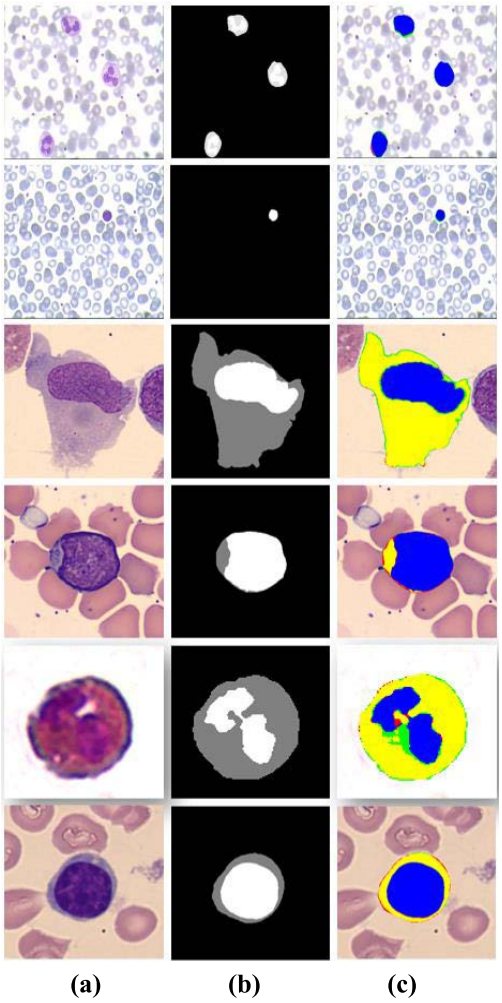

FIGURE 14. Sample images referring to challenges in WBC segmentation. (a) Original image, (b) ground-truth image, and (c) segmented images obtained using MIF-Net. (TP pixels for cytoplasm and nucleus segmentation are denoted by yellow and blue color, respectively. Moreover, FP pixels are represented by green and FN pixels are represented by red).

is likely to have a limitation of considering adjacent cells as a single cell for WBC count. To confirm this, we intend to work on WBCs segmentation for adjacent cells cases in the future.

4) LEUKEMIA DIAGNOSIS

Leukemia is one of the critical and common types of blood cancer that occurs due to the replication of anomalous WBCs. Acute myelogenous leukemia (AML), acute lymphoblastic leukemia (ALL), and chronic lymphocytic leukemia (CLL) are categorized as the common types of leukemia [31]. WBC count is attributed as one of the core biomarkers for the clinical diagnosis of leukemia [32]. Medical specialists normally perform manual assessments for checking the size, shape, position, and nuclear-cytoplasmic-ratio (NCR) of WBCs for leukemia diagnosis. Manual assessment is time-consuming, less accurate, and tedious. Therefore, we proposed a framework that can assist the leukemia diagnosis by providing automatic WBC segmentation and count. AML can be detected by identifying the large size and irregular shape nucleus [6] [33]. Likewise, another study states that size and shape assessment of cytoplasm and nucleus aids in categorizing the ALL and AML [31]. Smudged cells also play a key role in the detection of CLL. Subsequently, MIF-Net is proposed to exhibit all these anomalies associated with morphology and count through the WBC segmentation and computational assessment.

5) DIAGNOSIS OF COVID-19 AND OTHER INFECTIOUS DISEASES

WBC count and morphology have a vital role in the clinical diagnosis of many diseases like coronavirus disease 2019 (COVID-19), blood cancer, and other infections. COVID-19 has been declared a pandemic by the world health organization in 2019 because of its high transmissibility and fatality rate. It is evident from many studies, COVID-19 also brings significant changes in WBC's count and morphology [34]. These changes and anomalies associated with COVID-19 also vary with disease progression and intensity. COVID-19 patients are observed to have pyknosis which refers to shrinkage of the nucleus [35]. Similarly, some patients exhibit karyorrhexis in which some area of cytoplasm is covered by nuclear membrane because of its rupturing [35]. Reactive lymphocytes having larger cytoplasm is also commonly reported in COVID-19 patients [35], [36]. Many studies also testified to distorted neutrophils and smudged cells in COVID-19 patients [37]. Likewise, pseudo-pelger-Huet is also a common anomaly associated with COVID-19 [38]. Detection for all these anomalies is based on the segmentation performance of the nucleus and cytoplasm. Generally, WBC counting and morphological analysis are carried out manually which is an inaccurate and time-consuming process [7]. Therefore, proposed automatic WBC segmentation-based method can be used to aid the existing COVID-19 detection systems.

6) NCR

NCR is the ratio between the nucleus and cytoplasm area in a WBC. NCR is a key measure that provides computational analysis of WBC to assess maturity, malignancy, and morphology for the diagnosis of leukemia and other related diseases [38]. NCR is also associated with cell maturity since the nucleus area decreases with the course of cell maturity [38]. Similarly, leukemia patients exhibit some anomalies which change the shape and area of the cytoplasm. Therefore, pixel-wise predictions provide an accurate area for nucleus and cytoplasm which directly helps in precise NCR computations. In Figure 15, a sample segmented image from Dataset-1 is taken for calculating NCR. Mathematical calculation of NCR for the same image is given in Equation (10).

$$NCR = \frac{R_n}{R_c} = \frac{1945}{3403} = 0.571 \tag{10}$$

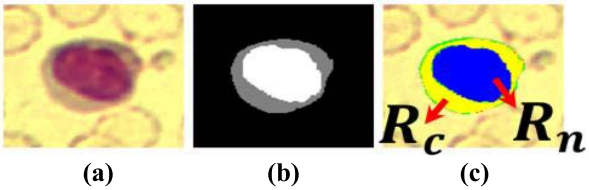

FIGURE 15. NCR computation for sample image of Dataset-1 using MIF-Net. (a) Input image. (b) Ground-truth image. (c) Segmented output image (Area of cytoplasm and nucleus is represented with R_c and R_n, respectively).

Along with many merits, MIF-Net has a few limitations as well. Since all four datasets of this study are having rare WBCs cases with NRBCs, therefore, we could evaluate only some sample NRBC cases. We intend to work on the segmentation of WBCs images with several NRBCs cases in the future.

VI. CONCLUSION

Leukemia is a fatal disease, its traditional diagnosis is based on manual assessments, which is a subjective, error-prone, and tedious process. To fill this gap, we developed MIF-Net for joint segmentation of cytoplasm and nucleus in WBC images. Leukemia brings changes in the count and morphology of WBC. MIF-Net is a shallow architecture that applies internal and external fusion to provide accurate WBC count and morphological predictions. Initial layers of CNN carry fine boundary information and MIF-Net fuses this boundary information with spatial features for enhancing the segmentation performance. MIF-Net is evaluated on four publicly available datasets and outperformed the existing state-of-the-art methods with superior computational efficiency. The proposed method can steadfastly assist the health experts and contribute to reducing the burden of the diagnostic sector.

In the future, we will work on segmentaion of adjacent cells. In addition, we will also consider other types of cancers for computer-assisted diagnosis.

REFERENCES

[1] X. Zheng, Y. Wang, G. Wang, and J. Liu, "Fast and robust segmentation of white blood cell images by self-supervised learning," *Micron*, vol. 107, pp. 55–71, Apr. 2018.

[2] *The Biologics News and Reports Portal*. Accessed: Sep. 14, 2021. [Online]. Available: https://tinyurl.com/mru4wr74

[3] L. H. Nee, M. Y. Mashor, and R. Hassan, "White blood cell segmentation for acute leukemia bone marrow images," *J. Med. Imag. Health Inform.*, vol. 2, no. 3, pp. 278–284, 2012.

[4] K. AL-Dulaimi, J. Banks, K. Nugyen, A. Al-Sabaawi, I. Tomeo-Reyes, and V. Chandran, "Segmentation of white blood cell, nucleus and cytoplasm in digital haematology microscope images: A review–challenges, current and future potential techniques," *IEEE Rev. Biomed. Eng.*, vol. 14, pp. 290–306, 2021.

[5] A. M. Abdeldaim, A. T. Sahlol, M. Elhoseny, and A. E. Hassanien, "Computer-aided acute lymphoblastic leukemia diagnosis system based on image analysis," in *Advances in Soft Computing and Machine Learning in Image Processing*. Guadalajara, Mexico: Springer, 2018, pp. 131–147.

[6] J. Su, S. Liu, and J. Song, "A segmentation method based on HMRF for the aided diagnosis of acute myeloid leukemia," *Comput. Methods Programs Biomed.*, vol. 152, pp. 115–123, Dec. 2017.

[7] S. N. M. Safuan, M. R. M. Tomari, and W. N. W. Zakaria, "White blood cell (WBC) counting analysis in blood smear images using various color segmentation methods," *Measurement*, vol. 116, pp. 543–555, Feb. 2018.

[8] V. V. Quinones, M. J. Macawile, A. Ballado, J. D. Cruz, and M. V. Caya, "Leukocyte segmentation and counting based on microscopic blood images using HSV saturation component with blob analysis," in *Proc. 3rd Int. Conf. Control Robot. Eng. (ICCRE)*, Apr. 2018, pp. 254–258.

[9] X. Zhou, C. Wang, Z. Li, and F. Zhang, "Adaptive histogram thresholding-based leukocyte image segmentation," in *Proc. 15th Int. Conf. Adv. Intell. Inf. Hiding Multimedia Signal Process.*, Jilin, China, Jul. 2020, pp. 451–459.

[10] H. Inbarani and A. T. Azar, "Leukemia image segmentation using a hybrid histogram-based soft covering rough K-Means clustering algorithm," *Electronics*, vol. 9, no. 1, p. 188, Jan. 2020.

[11] Z. Zhong, T. Wang, K. Zeng, X. Zhou, and Z. Li, "White blood cell segmentation via sparsity and geometry constraints," *IEEE Access*, vol. 7, pp. 167593–167604, 2019.

[12] S. Manasi, M. Ramyaa, N. Sri Madhava Raja, S. Arunmozhi, and S. C. Satapathy, "Segmentation and assessment of leukocytes using entropy-based procedure," in *Intelligent Data Engineering and Analytics*. Surathkal, India: Springer, 2021, pp. 691–699.

[13] A. Tareef, Y. Song, W. Cai, Y. Wang, D. D. Feng, and M. Chen, "Automatic nuclei and cytoplasm segmentation of leukocytes with color and texture-based image enhancement," in *Proc. IEEE 13th Int. Symp. Biomed. Imag. (ISBI)*, Apr. 2016, pp. 935–938.

[14] O. Sarrafzadeh, A. M. Dehnavi, H. Rabbani, and A. Talebi, "A simple and accurate method for white blood cells segmentation using K-means algorithm," in *Proc. IEEE Workshop Signal Process. Syst. (SiPS)*, Oct. 2015, pp. 1–6.

[15] S. Kadry, V. Rajinikanth, D. Taniar, R. Damaševičius, and X. P. Blanco, "Automated segmentation of leukocyte from hematological images-a study using various CNN schemes," *J. Supercomput.*, vol. 78, pp. 6974–6994, Nov. 2021.

[16] Y. Chen, S. Teng, and Z. Li, "Peripheral blood leukocyte image segmentation based on deep convolutional neural network," in *Proc. Int. Conf. Mach. Learn. Cyber Secur.*, Guangzhou, China, Oct. 2020, pp. 464–473.

[17] Y. Lu, H. Fan, and Z. Li, "Leukocyte segmentation via end-to-end learning of deep convolutional neural networks," in *Proc. 9th Int. Conf. Intell. Sci. Big Data Eng.*, Nanjing, China, Oct. 2019, pp. 191–200.

[18] K. K. Jha and H. S. Dutta, "Mutual information based hybrid model and deep learning for acute lymphocytic leukemia detection in single cell blood smear images," *Comput. Methods Programs Biomed.*, vol. 179, Oct. 2019, Art. no. 104987.

[19] N. Guo, L. Zeng, and Q. Wu, "A method based on multispectral imaging technique for white blood cell segmentation," *Comput. Biol. Med.*, vol. 37, no. 1, pp. 70–76, Jan. 2007.

[20] S. H. Rezatofighi and H. Soltanian-Zadeh, "Automatic recognition of five types of white blood cells in peripheral blood," *Computerized Med. Imag. Graph.*, vol. 35, no. 4, pp. 333–343, Jun. 2011.

[21] O. Ronneberger, P. Fischer, and T. Brox, "U-Net: Convolutional networks for biomedical image segmentation," in *Proc. Med. Image Comput. Comput.-Assist. Intervent*, 2015, pp. 234–241.

[22] V. Badrinarayanan, A. Handa, and R. Cipolla, "SegNet: A deep convolutional encoder-decoder architecture for robust semantic pixel-wise labelling," *IEEE Trans. Pattern Anal. Mach. Intell.*, vol. 39, no. 12, pp. 2481–2495, May 2017.

[23] P. Singh, P. Raj, and V. P. Namboodiri, "EDS pooling layer," *Image Vis. Comput.*, vol. 98, Jun. 2020, Art. no. 103923.

[24] D. P. Kingma and J. Ba, "Adam: A method for stochastic optimization," 2014, *arXiv:1412.6980*.

[25] H. Fan, F. Zhang, R. Wang, L. Xi, and Z. Li, "Correlation-aware deep generative model for unsupervised anomaly detection," in *Proc. 24th Conf. Adv. Knowl. Discovery Data Mining*, May 2020, pp. 688–700.

[26] W. A. Yasnoff, J. K. Mui, and J. W. Bacus, "Error measures for scene segmentation," *Pattern Recognit.*, vol. 9, no. 4, pp. 217–231, 1977.

[27] V. K. Singh, S. Romani, H. A. Rashwan, F. Akram, N. Pandey, M. Sarker, M. Kamal, S. Abdulwahab, J. Torrents-Barrena, A. Saleh, and M. Arquez, "Conditional generative adversarial and convolutional networks for X-ray breast mass segmentation and shape classification," in *Proc. 21st Int. Conf. Med. Image Comput. Comput. Assist. Intervent*, Granda, Spain, Sep. 2018, pp. 833–840.

[28] C. Zhou, H. Fan, and Z. Li, "TongueNet: Accurate localization and segmentation for tongue images using deep neural networks," *IEEE Access*, vol. 7, pp. 148779–148789, 2019.
[29] X. Zhou, Z. Li, H. Xie, T. Feng, Y. Lu, C. Wang, and R. Chen, "Leukocyte image segmentation based on adaptive histogram thresholding and contour detection," *Current Bioinf.*, vol. 15, no. 3, pp. 187–195, May 2020.
[30] R. R. Selvaraju, M. Cogswell, A. Das, R. Vedantam, D. Parikh, and D. Batra, "Grad-CAM: Visual explanations from deep networks via gradient-based localization," in *Proc. IEEE Int. Conf. Comput. Vis. (ICCV)*, Oct. 2017, pp. 618–626.
[31] N. H. A. Halim, M. Y. Mashor, and R. Hassan, "Automatic blasts counting for acute leukemia based on blood samples," *Int. J. Res. Comput. Sci.*, vol. 2, pp. 971–976, Aug. 2011.
[32] E. Suryani, W. Wiharto, and N. Polvonov, "Identification and counting white blood cells and red blood cells using image processing case study of leukemia," 2015, *arXiv:1511.04934*.
[33] S. Shinde, N. Sharma, P. Bansod, M. Singh, and C. K. Singh Tekam, "Automated nucleus segmentation of leukemia blast cells : Color spaces study," in *Proc. 2nd Int. Conf. Data, Eng. Appl. (IDEA)*, Feb. 2020, pp. 1–5.
[34] R. Mardani, A. A. Vasmehjani, F. Zali, A. Gholami, S. D. M. Nasab, H. Kaghazian, M. Kaviani, and N. Ahmadi, "Laboratory parameters in detection of COVID-19 patients with positive RT-PCR; a diagnostic accuracy study," *Arch. Acad. Emerg. Med.*, vol. 8, no. 1, pp. 1–5, 2020.
[35] I. Berber, O. Cagasar, A. Sarici, N. K. Berber, I. Aydogdu, O. Ulutas, A. Yildirim, H. G. G. Bag, and L. A. Delen, "Peripheral blood smear findings of COVID-19 patients provide information about the severity of the disease and the duration of hospital stay," *Med. J. Hematol. Infect. Dis.*, vol. 13, no. 1, pp. 1–10, 2021.
[36] O. Pozdnyakova, N. T. Connell, E. M. Battinelli, J. M. Connors, G. Fell, and A. S. Kim, "Clinical significance of CBC and WBC morphology in the diagnosis and clinical course of COVID-19 infection," *Amer. J. Clin. Pathol.*, vol. 155, no. 3, pp. 364–375, Feb. 2021.
[37] G. Kaur, F. Sandeep, O. Olayinka, and G. Gupta, "Morphologic changes in circulating blood cells of COVID-19 patients," *Cureus*, vol. 13, Feb. 2021, Art. no. e13416.
[38] A. Bodzas, P. Kodytek, and J. Zidek, "Automated detection of acute lymphoblastic leukemia from microscopic images based on human visual perception," *Frontiers Bioeng. Biotechnol.*, vol. 8, Aug. 2020, Art. no. 01005.
[39] L. H. S. Vogado, R. D. M. S. Veras, A. R. Andrade, R. R. V. E. Silva, F. H. D. D. Araujo, and F. N. S. De Medeiros, "Unsupervised leukemia cells segmentation based on multi-space color channels," in *Proc. IEEE Int. Symp. Multimedia (ISM)*, Dec. 2016, pp. 451–456.
[40] M. Makem and A. Tiedeu, "An efficient algorithm for detection of white blood cell nuclei using adaptive three stage PCA-based fusion," *Informat. Med. Unlocked*, vol. 20, Jan. 2020, Art. no. 100416.
[41] P. P. Banik, R. Saha, and K.-D. Kim, "An automatic nucleus segmentation and CNN model based classification method of white blood cell," *Expert Syst. Appl.*, vol. 149, Jul. 2020, Art. no. 113211.
[42] I. Vincent, K.-R. Kwon, S.-H. Lee, and K.-S. Moon, "Acute lymphoid leukemia classification using two-step neural network classifier," in *Proc. 21st Korea-Japan Joint Workshop Frontiers Comput. Vis. (FCV)*, Jan. 2015, pp. 254–258.
[43] X. Zheng, Y. Wang, and G. Wang, "White blood cell segmentation using expectation-maximization and automatic support vector machine learning," *Data Acquisition Process*, vol. 28, no. 5, pp. 614–619, 2013.
[44] C. Kong and S. Lucey, "Take it in your stride: Do we need striding in CNNs?" 2017, *arXiv:1712.02502*.
[45] S. D. Khan and S. Basalamah, "Multi-scale person localization with multi-stage deep sequential framework," *Int. J. Comput. Intell. Syst.*, vol. 14, p. 1875, Jan. 2021.
[46] S. D. Khan, L. Alarabi, and S. Basalamah, "A unified deep learning framework of multi-scale detectors for geo-spatial object detection in high-resolution satellite images," *Arabian J. Sci. Eng.*, Oct. 2021, doi: 10.1007/s13369-021-06288-x.
[47] S. Arslan, E. Ozyurek, and C. Gunduz-Demir, "A color and shape based algorithm for segmentation of white blood cells in peripheral blood and bone marrow images," *Cytometry A*, vol. 85, no. 6, pp. 480–490, 2014.
[48] E. Shelhamer, J. Long, and T. Darrell, "Fully convolutional networks for semantic segmentation," *IEEE Trans. Pattern Anal. Mach. Intell.*, vol. 39, no. 4, pp. 640–651, Apr. 2017.
[49] H. Fan, F. Zhang, L. Xi, Z. Li, G. Liu, and Y. Xu, "LeukocyteMask: An automated localization and segmentation method for leukocyte in blood smear images using deep neural networks," *J. Biophotonics*, vol. 12, no. 7, Jul. 2019, Art. no. e201800488.

NADEEM AKRAM received the M.B.B.S. degree from the University of Health Sciences, Lahore. He is currently working as a Medical Officer at the Department of Primary and Secondary Health Care, Government of Pakistan. His research interest includes study on computer-aided-diagnosis of cancer.

SHARJEEL ADNAN received the M.B.B.S. degree from the University of Health Sciences, Lahore. He is currently working as a Medical Officer with the Department of Primary and Secondary Health Care, Government of Pakistan. His research interest includes computational methods for the diagnosis of different types of cancer.

MUHAMMAD ASIF received the M.B.B.S. degree from Chongqing Medical University, China. He is currently working as a Medical Officer with the Department of Primary and Secondary Healthcare, Government of Pakistan. His research interests include leukemia, Hodgkin lymphoma, and non-Hodgkin lymphoma.

SYED MUHAMMAD ALI IMRAN received the B.Sc. degree in computer system engineering from the NFC Institute of Engineering and Technology Multan, Pakistan, in 2011, and the M.S. degree in computer science from the National College of Business Administration and Economics (NCBAE), Lahore, Pakistan, in 2016. He is currently pursuing the Ph.D. degree in computer science with Superior University Gold Campus, Lahore. Since 2017, he has been a Lecturer at the University of Agriculture, Faisalabad. His research interests include image processing and deep learning for disease diagnosis.

MUHAMMAD NAVEED YASIR received the B.Sc. degree in computer engineering from the COMSATS Institute of Information Technology, Pakistan, in 2008, the master's degree in control systems engineering from The University of Sheffield, U.K., in 2010, and the Ph.D. degree in engineering from Dongguk University, Seoul, South Korea, in 2018. He has worked as an Assistant Professor at The University of Lahore, Lahore, from 2018 to 2019, and a Lecturer at Bahauddin Zakariya University, Multan. He has also worked as an Assistant Professor with the Department of Computer Engineering, Khwaja Fareed University of Engineering and Information Technology (KFUEIT), Rahim Yar Khan. He is currently working as an Assistant Professor with the Department of Computer Science, University of Narowal, Narowal. His research interests include control systems, condition monitoring, machine learning, computer vision, artificial intelligence, and signal processing techniques.

RIZWAN ALI NAQVI received the B.S. degree in computer engineering from COMSATS University, Pakistan, in 2008, the M.S. degree in electrical engineering from Karlstad University, Sweden, in 2011, and the Ph.D. degree in electronics and electrical engineering from Dongguk University, South Korea, in 2018. From 2011 to 2012, he was a Lecturer with the Department of Computer Science, Sharif College of Engineering and Technology, Pakistan. He joined the Faculty of Engineering and Technology, Superior College, Pakistan, as a Senior Lecturer, in 2012. From 2018 to 2019, he worked as a Postdoctoral Researcher with Gachon University, South Korea. He is currently working as an Assistant Professor with Sejong University, South Korea. His research interests include gaze tracking, biometrics, computer vision, artificial intelligence, machine learning, deep learning, and medical imaging analysis.

DILDAR HUSSAIN received the B.S. degree in computer science from the Kohat University of Science and Technology, Pakistan, in 2010, and the Ph.D. degree in biomedical engineering from Kyung Hee University, South Korea, in 2019. From 2013 to 2019, he worked as a Research and Development Engineer with YOZMA BMTech Company Ltd., South Korea (develop diagnostic imaging equipment instruments, such as DXA, Chats X-rays, and Ultrasonic). He is currently working as a Postdoctoral Research Fellow with the School of Computational Science, Korea Institute for Advanced Study (KIAS), which is a subordinate institute of KAIST, South Korea. His research interests include bioinformatics, medical imaging, medical image analysis, computer vision, biomedical natural image processing, artificial intelligence, machine learning, deep learning, mineral, and nutritional study.